

Polarizable and Nonpolarizable Force Fields for Alkyl Nitrates

Oleg Borodin,^{*,†,‡} Grant D. Smith,^{†,‡} Thomas D. Sewell,[§] and Dmitry Bedrov^{†,‡}

Wasatch Molecular Incorporated, 2141 East St. Mary's Drive, Salt Lake City, Utah 84108, Department of Materials Science & Engineering, 122 South Central Campus Drive, Room 304, University of Utah, Salt Lake City, Utah 84112-0560, and Theoretical Division, Los Alamos National Laboratory, Los Alamos, New Mexico 87545

Received: August 1, 2007; In Final Form: October 17, 2007

Quantum-chemistry-based many-body polarizable and two-body nonpolarizable atomic force fields were developed for alkyl nitrate liquids and pentaerythritol tetranitrate (PETN) crystal. Bonding, bending, and torsional parameters, partial charges, and atomic polarizabilities for the polarizable force field were determined from gas-phase quantum chemistry calculations for alkyl nitrate oligomers and PETN performed at the MP2/aug-cc-pvDz level of theory. Partial charges for the nonpolarizable force field were determined by fitting the dipole moments and electrostatic potential to values for PETN molecules in the crystal phase obtained from molecular dynamics simulations using the polarizable force field. Molecular dynamics simulations of alkyl nitrate liquids and two polymorphs of PETN crystal demonstrate the ability of the quantum-chemistry-based force fields to accurately predict thermophysical and mechanical properties of these materials.

I. Introduction

Development of reliable tools for the prediction of thermophysical properties of the constituent materials used in energetic formulations is an important complement to experimental programs aimed at testing and optimization of materials for munitions, warhead, and propellant applications.¹ Classical molecular dynamics (MD) simulations are useful for predicting deformation processes and pressure- and temperature-dependent structures and properties of energetic materials over a wide range of thermodynamic conditions, including ones that are exceedingly difficult to probe experimentally due to violent reactivity of these materials above certain critical values.^{1–5}

The objective of the present study is to develop and validate quantum-chemistry-based force fields for the prediction of temperature- and pressure-dependent properties of pentaerythritol tetranitrate (PETN) and related alkyl nitrate materials. An assessment of previous atomistic simulation studies of PETN^{1,6–9} convinced us that none of the existing force fields are sufficiently accurate to predict simultaneously the pressure dependence of unit cell parameters of the two atmospheric-pressure-stable crystal polymorphs, the heat of sublimation, the heat of fusion, and the ambient pressure second-order elastic coefficients of PETN with the desired accuracy. A rigid-molecule force field⁹ for the relatively flexible PETN molecule was successful for describing cell parameters at room temperature but predicted a bulk modulus 40% higher than experiment. It also predicted a much weaker pressure dependence of cell parameters. These shortcomings have been attributed to the rigid representation of PETN molecules.⁹ Fully flexible PETN force fields such as the COMPASS force field,⁶ which appears to be the most accurate and fully tested of the published force fields for PETN,^{1,6–9} still leave room for improvement. Specifically, while the PETN lattice parameters at room temperature are accurately

reproduced by this potential, the heat of sublimation is 12.6% higher than experimental values.^{10,11} Similarly, the COMPASS force field predicts an accurate bulk modulus,¹² but individual elastic coefficients are in error by up to 108% compared with experimental¹³ values. Also, this force field has a well depth parameter for the Lennard-Jones nonbonded interactions (ϵ) between nitrate oxygen atoms (see Figure 1 for designation of atom types) that is four times larger than the well depth for interactions between the nitro oxygen atoms. This difference stands out significantly compared with previously suggested generalized Lennard-Jones parameters.¹⁴ The Lennard-Jones well depth (ϵ) for the nitro group oxygen was optimized in the COMPASS force field to a value of 0.048 kcal/mol, which is three times smaller than the value of 0.17 kcal/mol obtained for the OPLS-AA force field. Such large differences between Lennard-Jones parameters are not typical.

Another flexible PETN force field attributed to Ye et al.⁷ accurately reproduced the crystal lattice energy (to better than 0.2%) but significantly overestimated the lattice parameter c ; its value obtained from energy minimization (i.e., the zero Kelvin structure) was 4% larger than the experimental value at room temperature. Zaoui and Sekkal⁸ used a three-body potential in a Tersoff form that was adjusted to match PETN properties including lattice parameters and bulk modulus; however, their simulations were short (0.02 ns), and the simulation cell used consisted of only 256 atoms. These simulation details, plus the fact that the stated number of atoms does not correspond to an integral number of PETN molecules, cast doubt on the reliability of their results. Finally, we note that Gee et al.¹² parametrized a coarse-grained model in which each PETN molecule was mapped onto five beads, one bead for C(CH₂O)₄ plus four beads representing the pendent NO₂ groups, that accurately reproduced crystal lattice parameters, bulk modulus, and sublimation energy.

In an effort to develop a more reliable and transferable force field for PETN and other alkyl nitrates, we used a force field development methodology that includes two principal steps. The first step involves development of a many-body polarizable force

* Corresponding author. E-mail: Oleg.Borodin@utah.edu.

[†] Wasatch Molecular Incorporated.

[‡] University of Utah.

[§] Los Alamos National Laboratory.

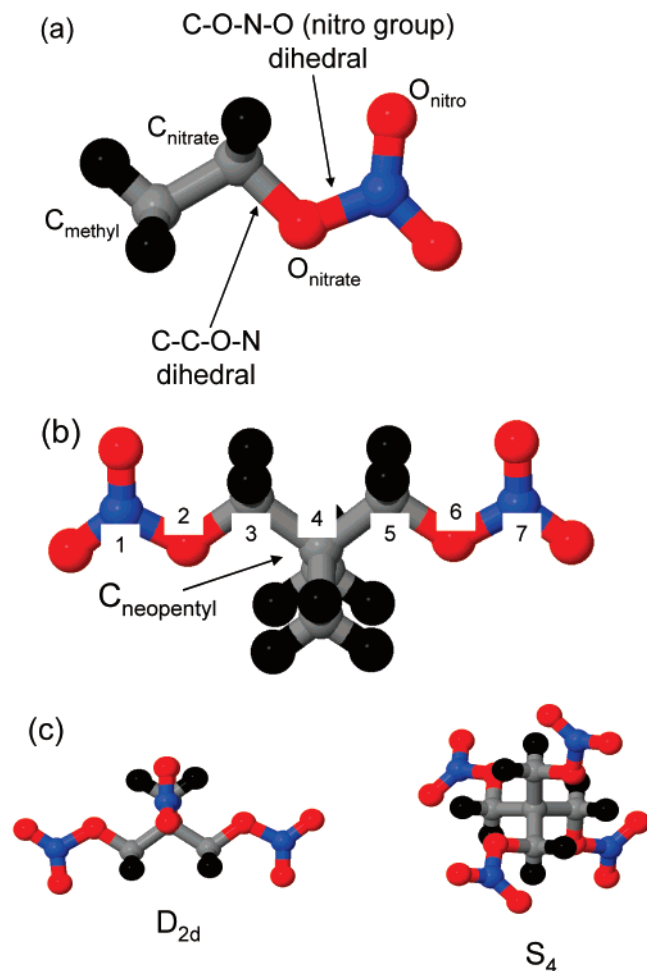


Figure 1. (a) Ethyl nitrate, (b) 2,2-dimethyl-1,3-propanediol dinitrate (DMPDN), and (c) PETN.

field based on electrostatic potential, polarization, and conformational structures and energies obtained from quantum chemistry calculations for alkyl nitrates and PETN. Polarizable potentials have proven to be more transferable between related compounds than two-body potentials.^{15,16} Furthermore, since polarizable potentials take into account explicitly the influence of condensed-phase effects on electrostatic interactions, such a potential, parametrized to reproduce gas-phase electrostatics, should accurately represent electrostatic interactions in solid and liquid phases. The second step involves parametrization of a nonpolarizable two-body force field based on simulation results for PETN crystal performed using the polarizable force field. Here, the partial charges for the nonpolarizable force field are parametrized to describe the electrostatic potential and molecular dipole moment in PETN crystal rather than from gas-phase results.

II. Quantum Chemistry Studies

Quantum chemistry studies were conducted on ethyl nitrate (Figure 1a), 2,2-dimethyl-1,3-propanediol dinitrate (DMPDN, Figure 1b), and the two low-energy, high-symmetry conformers of PETN (Figure 1c). Gaussian98 was used in all calculations.¹⁷ Geometry optimizations for each of these compounds were performed using density functional theory (DFT) at the mPW1PW91/aug-cc-pvDz level of theory. The mPW1PW91 density functional was chosen because of its ability to predict weak interactions, dipole–dipole interactions, and hydrogen bonding more accurately than other commonly used density

TABLE 1: Relative Energies (Kilocalories per Mole) of Two High-Symmetry PETN Conformers

conformer	B3LYP/ 6-311+G(d,p) ¹⁹	mPW1PW91/ Dz ^a	HF/ Dz ^a	MP2/ Dz ^a	polarizable force field ^b
<i>S</i> ₄	0	0	0	0	0
<i>D</i> _{2d}	0.34	0.12	−0.05	−0.07	0.26

^a Using an aug-cc-pvDz basis set with mPW1PW91/aug-cc-pvDz geometries. ^b Energy obtained from molecular mechanics calculations using the quantum-chemistry-based polarizable force field at the molecular-mechanics-optimized geometry.

functionals such as B3LYP.¹⁸ Single-point energies for the mPW1PW91/aug-cc-pvDz optimized geometries were calculated using mPW1PW91/aug-cc-pvDz, HF/aug-cc-pvDz, and MP2/aug-cc-pvDz.

For ethyl nitrate, energy scans about the C–C–O–N and C–O–N–O (nitro group rotation) dihedrals, denoted in Figure 1a, were performed with all degrees of freedom optimized but the dihedral of interest. Energies as a function of distortion of the O_{nitro}–N–O_{nitro} bend angle and O–N*–O–O out-of-plane bending angle were also determined and are reported in Supporting Information (Table S1). The relative conformational energies and dihedral geometries for ethyl nitrate were found to be similar to previously reported values⁶ obtained using smaller basis sets; the former are given in Supporting Information (Table S2). Geometries and energies of the minimum and first-order saddle-point for rotation about the C–C–C–O dihedral in DMPDN were also determined (Table S3, Supporting Information).

The relative energies of the optimized *S*₄ and *D*_{2d} conformers of PETN (Figure 1c) are given in Table 1. These conformers are essentially isoenergetic in the gas phase. The relative conformational energy (*D*_{2d} vs *S*₄) calculated using mPW1PW91/aug-cc-pvDz is 0.12 kcal/mol; this is somewhat lower than the value of 0.34 kcal/mol obtained from DFT calculations by Gruzdkov et al.¹⁹ at the B3LYP/6-311+G(d,p) level of theory. As the mPW1PW91 density functional is known¹⁸ to be more reliable than B3LYP in predicting dipole–dipole and weak interactions, the former functional is expected to provide more accurate results, and indeed, the mPW1PW91/aug-cc-pvDz numbers are closer to the MP2/aug-cc-pvDz predictions which we consider to be the most accurate.

III. Polarizable Force Field Development

A. Form of the Potential-Energy Function. Following our previous work on developing force fields for liquids^{15,20,21} and polymers,²² we used the form of the potential energy function $U^{\text{tot}}(\mathbf{r})$ for an ensemble of atoms represented by the coordinate vector \mathbf{r} and given by

$$U^{\text{tot}}(\mathbf{r}) = U^{\text{NB}}(\mathbf{r}) + \sum_{\text{bonds}} U^{\text{BOND}}(r_{ij}) + \sum_{\text{bonds}} U^{\text{BEND}}(\theta_{ijk}) + \sum_{\text{dihedrals}} U^{\text{DIHEDRAL}}(\phi_{ijkl}) + \sum_{\text{improper dihedrals}} U^{\text{IMP}}(\phi_{ijkl}^{\text{imp}}) \quad (1)$$

where the sums are over each bond, bend, dihedral, and improper dihedral in the system. The contributions to the potential energy due to bonds, bends, dihedrals, and out-of-plane bending (improper dihedrals) are

$$U^{\text{BOND}}(r_{ij}) = \frac{1}{2} k_{\alpha\beta}^{\text{BOND}} (r_{ij} - r_{ij}^0)^2 \quad (2)$$

$$U^{\text{BEND}}(\theta_{ijk}) = \frac{1}{2} k_{\alpha\beta\gamma}^{\text{BEND}} (\theta_{ijk} - \theta_{ijk}^0)^2 \quad (3)$$

$$U^{\text{DIHEDRAL}}(\phi_{ijkl}) = \sum_n \frac{1}{2} k_{\alpha\beta\gamma\delta,n}^{\text{DIHEDRAL}} [1 - \cos(n\phi_{ijkl})] \quad (4)$$

$$U^{\text{IMP}}(\phi_{ijkl}^{\text{imp}}) = (1/2) k_{\alpha\beta\gamma\delta}^{\text{IMP}} (\phi_{ijkl}^{\text{imp}})^2 \quad (5)$$

where r_{ij} and r_{ij}^0 are the instantaneous and “natural” bonding distances for atoms i and j ; θ_{ijk} and θ_{ijk}^0 are the instantaneous and “natural” bending angles for atoms i , j and k ; ϕ_{ijkl} is the dihedral angle for atoms i , j , k and l ; and ϕ_{ijkl}^{imp} is the out-of-plane bending angle for an sp^2 center at atom j . These interactions have corresponding force constants $k_{\alpha\beta}^{\text{BOND}}$, $k_{\alpha\beta\gamma}^{\text{BEND}}$, $k_{\alpha\beta\gamma\delta,n}^{\text{DIHEDRAL}}$, and $k_{\alpha\beta\gamma\delta}^{\text{IMP}}$, respectively. The subscripts α , β , γ , and δ denote atom type for atoms i , j , k , and l , respectively.

The nonbonded energy $U^{\text{NB}}(\mathbf{r})$ consists of the sum of two-body repulsion and dispersion energy terms $U^{\text{RD}}(\mathbf{r})$, the energy due to interactions of fixed charges $U^{\text{coul}}(\mathbf{r})$, and the polarization energy $U^{\text{pol}}(\mathbf{r})$ arising from the interaction between induced dipoles with fixed charges and other induced dipoles:

$$U^{\text{NB}}(\mathbf{r}) = U^{\text{RD}}(\mathbf{r}) + U^{\text{coul}}(\mathbf{r}) + U^{\text{pol}}(\mathbf{r}) = \sum_{i>j} \left(A_{\alpha\beta} \exp(-B_{\alpha\beta} r_{ij}) - C_{\alpha\beta} r_{ij}^{-6} + D \left(\frac{12}{B_{\alpha\beta} r_{ij}} \right)^{12} \right) + \sum_{i>j} \left(\frac{q_i q_j}{4\pi\epsilon_0 r_{ij}} \right) - 0.5 \sum_i \bar{\mu}_i \bar{E}_i^0 \quad (6)$$

The induced dipole at force center i is $\bar{\mu}_i = \alpha_i \bar{E}_i^{\text{tot}}$; α_i is the isotropic atomic polarizability; \bar{E}_i^{tot} is the total electrostatic field at the atomic site i due to permanent charges q_j and induced dipoles $\bar{\mu}_j$; ϵ_0 is the dielectric permittivity of vacuum; \bar{E}_i^0 is the electric field due to fixed charges only; $A_{\alpha\beta}$ and $B_{\alpha\beta}$ are the repulsion parameters, and $C_{\alpha\beta}$ is the dispersion parameter for interaction between atoms i and j with atom types α and β . The term $D(12/B_{\alpha\beta} r_{ij})^{12}$, with $D = 5 \times 10^{-5}$ kcal/mol for all pair interactions, is essentially zero at typical nonbonded atomic separations but becomes the dominant term at $r_{ij} < 1$ Å, ensuring that $U^{\text{RD}}(\mathbf{r})$ is repulsive at distances much smaller than the size of an atom. Nonbonded interactions are included for atoms separated by three or more covalent bonds. We used Thole screening¹⁵ ($a_T = 0.4$) that smears induced dipoles in order to prevent a “polarization catastrophe” from occurring. The interaction between an induced dipole and a partial charge separated by 3 bonds was scaled by 0.8. Finally, for heteroatom interactions, the modified Waldman–Hagler combining rules¹⁵ were used

$$A_{ij} = \sqrt{A_i A_j} \frac{B_{ij}^6}{B_{ii}^3 B_{jj}^3} \quad B_{ij} = \left(\frac{2}{B_{ii}^{-6} + B_{jj}^{-6}} \right)^{1/6} \quad C_{ij} = \sqrt{C_i C_j} \quad (7)$$

B. Force Field Fitting for the Polarizable Potential. We followed a previously described force field development methodology^{15,23} that will only be briefly summarized here. First, atomic polarizabilities are determined by fitting to the molecular polarizability of gas-phase molecules as determined from quantum chemistry. Second, partial charges are fit to describe the electrostatic potential on a grid of points around a molecule, as well as molecular gas-phase dipole and quadrupole moments, all obtained from quantum chemistry. Third, bond lengths and natural bending angles are fit to reproduce geometries of gas-phase molecules obtained from quantum chemistry, while

bending force constants are either taken from previously developed force fields or fit to the energetics of bending angle distortions obtained from quantum chemistry. Finally, torsional parameters are determined by fitting the gas-phase conformational-energy surface of model molecules as determined from quantum chemistry.

Atomic Polarizabilities. Atomic polarizabilities of hydrogen and carbon atoms were transferred from a previously developed force field for alkanes and ethers;²⁴ these are similar to the values used in our previous work.¹⁵ The atomic polarizabilities of oxygen and nitrogen atoms are expected to be similar to each other on the basis of our previous studies¹⁵ and were fit to the molecular polarizability of ethyl nitrate obtained at the MP2/aug-cc-pvDz//mPW1PW91/aug-cc-pvDz level of theory. The assigned atomic polarizabilities are given in Table 2.

Partial Atomic Charges. In order to establish partial atomic charges for the polarizable potential, the electrostatic potentials on grids of evenly spaced points ($\sim 10^5$ points) around the two low-energy gas-phase conformers of ethyl nitrate ($\phi_{\text{CCON}} = 180^\circ$ and 81.2°) and PETN (S_4 point group), as well as the dipole moments $\bar{\mu}_i$ and the quadrupole moments Θ_i of these molecules, were calculated at the MP2/aug-cc-pvDz//mPW1PW91/aug-cc-pvDz level of theory. Charge-bond increments were used to calculate partial atomic charges. The value q_i of the partial charge positioned on atom i is calculated as a sum of all charge-bond increments that involve atom i , as shown in eq 8.

$$q_i = \sum_j^{n\text{Bonds}} \delta_{ij} \quad (8)$$

A set of charge-bond increments ($\bar{\delta}$) was determined by minimizing the objective function

$$\chi^2(\bar{\delta}) = \sum_{i=1}^M \left[\sum_{j=1}^{N_{\text{GRID}}} \frac{\omega^\phi}{N_{\text{GRID}}} (\phi_{ij}^{\text{QC}} - \phi_{ij}^{\text{FF}}(\bar{\delta}))^2 + \omega(\bar{\mu}_i^{\text{QC}} - \bar{\mu}_i^{\text{FF}}(\bar{\delta}))^2 + \omega^\Theta (\Theta_i^{\text{QC}} - \Theta_i^{\text{FF}}(\bar{\delta}))^2 \right] \quad (9)$$

where ϕ_{ij}^{QC} and ϕ_{ij}^{FF} are the electrostatic potential for the i th molecule (or complex) at the j th grid point from quantum chemistry (QC) and the developed force field (FF), respectively; $\bar{\mu}_i^{\text{QC}}$ and $\bar{\mu}_i^{\text{FF}}$ are dipole moments for molecule i , and Θ_i^{QC} and Θ_i^{FF} are quadrupole moments for molecule i . The relative weights for fitting electrostatic potential, dipole, and quadrupole moments ω^ϕ , ω^μ , ω^Θ were set to 1.0, 0.1, and 0.05, respectively. The electrostatic potential for points closer than 1.8 Å to oxygen, 1.5 Å to hydrogen, 2.5 Å to carbon, and 2.2 Å to nitrogen atoms were excluded from the fitting, as were points further than 4 Å from any atom. The optimized charge-bond increments are given in Table 3. The root-mean-square deviation of the electrostatic potential calculated using the optimized force field parameters from quantum chemistry calculations is 1.1 kcal/mol for PETN and 1.4 kcal/mol for ethyl nitrate.

Repulsion-Dispersion Parameters. All repulsion-dispersion parameters were transferred without modification from our previously developed force fields²⁴ for ethers, alkanes, and carbonates. Repulsion-dispersion parameters for the polarizable force field are given in Table 2.

Valence Bonds. Bond lengths were fit to the values in the C–C–O–N = 180° conformer of ethyl nitrate and the S_4 conformer of PETN obtained at the mPW1PW91/aug-cc-pvDz level of theory. Bond lengths are given in Table 4. In all molecular mechanics calculations, the bonds were constrained

TABLE 2: Nonbonded Interactions for the Polarizable Potential for Alkyl Nitrates and PETN

element of pair	type	A (kcal/mol)	B (Å ⁻¹)	C (kcal Å ⁶ /mol)	mass (g/mol)	charge (e)	polarizability (Å ³)
C	neopentyl	97431	3.622	519.9	12.011	-0.2972	1.05
C	nitrate	97431	3.622	519.9	12.011	0.1308	0.70
C	methyl	97431	3.622	519.9	12.011	0 ^a , 0.1414 ^b	1.05
H		5352	4.365	22.6	1.008	0.1063	0.35
O	nitro	30906	3.881	213.9	15.999	-0.3856	1.00
O	nitrate	30906	3.881	213.9	15.999	-0.2879	1.00
N		39092	3.316	833.5	14.007	0.7900	0.90

^a In butyl nitrate and longer alkyl nitrates. ^b In ethyl nitrate.

TABLE 3: Charge-Bond Increments for the Polarizable Potential for Alkyl Nitrates and PETN

bond ^a	δ_{ij} (e) = $-\delta_{ji}$ (e)
(O)–C _i –C _j –(C) ₃	0.0743
(H) ₃ –C _i –C _j –(O)	0.1414
C _i –H _j in methyl group	0
(C)–C _i –C _j –(C)	0
H–C(H)–(O)	0.1063
(C)–C _i (H) ₂ –O _j –(N)	0.2691
(C) ₂ –C _i (H)–O _j –(N)	0.2691
N _i –O _{j,nitrate}	0.0188
N _i –O _{j,nitro}	0.3856

^a Atoms connected to the bond-increment atoms are given in parentheses.

to the values given in Table 4. As shown in Table 4, the C–C, C–O, and N–O_{nitrate} bond lengths lie between reported values for PETN-I and PETN-II obtained from X-ray diffraction. The N–O_{nitro} bond length is slightly shorter than those reported for PETN polymorphs obtained from X-ray diffraction.

Valence Bends. Natural bending angles (θ^0) were fit to reproduce the equilibrium geometry of ethyl nitrate (C–C–O–N = 180°) and PETN (*S*₄) obtained at the mPW1PW91/aug-cc-pvDz level of theory. Most of the bending force constants were transferred without modification from previous force fields.¹⁵ All natural bending angles and bending force constants are given in Table 4. The O–N–O bending force constant was fitted to the energy of planar distortion of the nitrate group assuming that the force constants for O_{nitrate}–N–O_{nitro} and O_{nitro}–N–O_{nitro} are equal. A comparison between quantum chemistry and force field predictions for the energies of the distorted nitrate group is provided in Table S1 in Supporting Information.

Out-of-Plane Bending Potentials. The out-of-plane bending potential for the nitrate group was determined by fitting to the relative energy of ethyl nitrate as a function of the out-of-plane bending angle. The resulting out-of-plane bending force constant is given in Table 4. A comparison between quantum chemistry and force field predictions for relative energies of ethyl nitrate as a function of the out-of-plane bending angle is shown in Table S1 and Figure S1 in Supporting Information.

Dihedral Potentials. Dihedral potentials were determined by fitting to the relative energy of rotation about the C–O–N–O and C–C–O–N dihedrals in ethyl nitrate and the C–C–C–O dihedral in DMPDN. The resulting dihedral parameters are given in Table 4; complete comparisons between quantum chemistry and force field predictions for the conformational energies and geometries in these compounds are given in Table S2, Table S3, and Figure S1 in Supporting Information. The ability of the force field to predict the relative conformational energies of two high-symmetry PETN conformers obtained from quantum chemistry calculations is shown in Table 1.

IV. Molecular Dynamics Simulation Methodology

Polarizable and nonpolarizable versions of the MD simulation code Lucretius²⁵ were used for all MD simulations of alkyl

nitrates and PETN crystals. The number of molecules in the liquid simulations is summarized in Table 5. For the low-temperature PETN crystal polymorph PETN-I (tetragonal space group)²⁶ and the high-temperature polymorph PETN-II (orthorhombic space group),²⁶ simulation cells containing 160 and 216 molecules, respectively, were employed. Periodic boundary conditions were used in all simulations. Most simulations were performed with bond lengths constrained using the SHAKE algorithm²⁷ in order to allow a larger time step; four simulations corresponding to pressures of 0, 3, 6, and 9 GPa were performed using unconstrained bonds in order to assess the influence of this approximation. All results reported below refer to simulations using constrained bonds unless otherwise noted. The Ewald summation method was used for the treatment of long-range electrostatic forces between partial charges and between partial charges and induced dipoles. The number of reciprocal vectors in the Ewald sum was 5³ and 6³ for cells containing 160 and 216 molecules, respectively; and the Ewald α parameter was equal to 0.233*/*L*, where *L* is the linear dimension of the simulation cell. A tapering function was used to drive the induced dipole–induced dipole interactions to zero at a cutoff of 11 Å, with scaling starting at 10 Å. A multiple-time-step, reversible reference-system-propagator algorithm was employed.²⁸ For simulations with constrained bonds, the following time steps were used: 0.5 fs for bending and torsional motions, 1.5 fs for nonbonded interactions within a 6.5 Å sphere, and 3.0 fs for nonbonded interactions between 6.0 Å and 11.0 Å and the reciprocal-space part of the Ewald summation.²⁷ For simulations with unconstrained bonds, the time steps were 0.25 fs for bonding, bending, and torsional motions; 1.0 fs for nonbonded interactions within a 6.5 Å sphere; and 2.0 fs for nonbonded interactions between 6.0 Å and 11.0 Å and the reciprocal-space part of the Ewald summation. All 1–4 interactions between partial charges and induced dipoles were scaled by a factor of 0.8; 1–4 Coulomb, repulsion and dispersion interactions were not scaled.

A Nose–Hoover thermostat and barostat²⁵ were used to control the temperature and pressure in all liquid simulations as well as in crystal phase simulations for the polarizable potential. For the latter, three independent barostats were employed and the system was constrained to orthorhombic symmetry (i.e., all three lattice angles were fixed at 90°). Simulation cells for the liquid were created at low density with an initial periodic cell (box) length of 60 Å. The density was then increased using Brownian dynamics simulations²⁷ over a period of 0.2 ns at 298 K for alkyl nitrates and at 416 K for PETN liquid in order to yield liquid densities, with subsequent equilibration in the isothermal–isobaric (NPT) ensemble for 0.4 ns at 298 K for alkyl nitrates and for 0.2 ns at 416 K for PETN liquid. Next, the temperature was changed to the target temperature values reported in Table 5 and simulations in the NPT ensemble were performed for the durations reported in Table 5. PETN crystal simulations using the polarizable potential were started from the experimental crystal structure determi-

TABLE 4: Bonding, Bending and Torsional Parameters for Alkyl Nitrates and PETN

bonds					
bond	$k_{\alpha\beta}^{\text{BOND}}$ (kcal/mol/Å ²)	r^0 (Å)	$r_{\text{constrained}}$ (Å)	exp (PETN-I) ²⁶ (Å)	exp (PETN-II) ²⁶ (Å)
C–C	618	1.521	1.530	1.537	1.537–1.539
C–H	655	1.093	1.100	1.05	1.03–1.04
C–O	739	1.423	1.445	1.462	1.433
N–O _{nitrate}	600	1.390	1.390	1.404	1.386–1.392
N–O _{nitro}	1530	1.200	1.200	1.203–1.225	1.203–1.229

bends					
bend	$k_{\alpha\beta\gamma}^{\text{BEND}}$ (kcal/mol/rad ²)	θ^0 (degrees)	bend	$k_{\alpha\beta\gamma}^{\text{BEND}}$ (kcal/mol/rad ²)	θ^0 (degrees)
C–C–C	108	112.0	C–C–O	172	105.3
C–C–H	86	110.0	H–C–H	77	108.2
C–C–H (–CH ₃)	86	110.5	H–C–H (–CH ₃)	77	107.7
H–C–O	112	106.7	O _{nitrate} –N–O _{nitro}	210	115.0
C–O–N	111	109.6	O _{nitro} –N–O _{nitro}	210	130.0

dihedrals and out-of-plane bending					
dihedral	$k_{\alpha\beta\gamma\delta,0}^{\text{DIHEDRAL}}$ (kcal/mol)	$k_{\alpha\beta\gamma\delta,1}^{\text{DIHEDRAL}}$ (kcal/mol)	$k_{\alpha\beta\gamma\delta,2}^{\text{DIHEDRAL}}$ (kcal/mol)	$k_{\alpha\beta\gamma\delta,3}^{\text{DIHEDRAL}}$ (kcal/mol)	$k_{\alpha\beta\gamma\delta}^{\text{IMP}}$ (kcal/mol)
C–C–C–H	0.00	0.00	0.00	–0.30	N/A
C–C–C–O	0.00	0.00	0.00	–0.20	N/A
C–C–O–N	0.00	0.62	–0.72	–1.63	N/A
H–C–O–N	0.00	0.00	0.00	–0.30	N/A
C–O–N–O	0.00	0.00	4.18	0.00	N/A
O–N*–O–O ^a	N/A	N/A	N/A	N/A	68.4 ^a

^a Single out-of-plane bending function is associated with each nitrate group.

TABLE 5: Density, Heat of Vaporization and Self-diffusion Coefficient of Alkyl Nitrate and PETN Liquids

compound	N^a	time ^b (ns)	T (K)	ρ (kg m ^{–3})		ΔH^{vap} (kcal/mol)		D (10 ^{–10} m ² /s)
				MD	expt	MD	expt	
ethyl nitrate	288	0.4	293	1102	1108 ^c	8.17	8.67 ^f	23
butyl nitrate	216	0.4	293	1026		10.37		12
butyl nitrate	216	0.4	298	1020	1023 ^d	10.26	10.42 ^f	13.5
isopropyl nitrate	216	0.5	293	1060	1034 ^e	8.63	9.27 ^f	15.7
PETN liquid	160	0.4	416	1500				

^a Number of molecules in the simulation cell. ^b Length of NPT simulations. ^c Reference 35. ^d Measured value at 303 K from ref 35. ^e Measured value at 292 K from ref 35. ^f Taken from NIST Webbook that cites ref 36.

nation. Equilibration under NPT conditions was performed for 0.2 ns and followed by production NPT runs of length 0.4 ns.

In simulations using the nonpolarizable potential, a fully triclinic hybrid MD–MC (Monte Carlo) approach used in our previous simulations of crystals of energetic materials was employed.² Specifically, a 100 fs trajectory segment of isothermal-isochoric MD (NVT–MD) was followed by 10 attempted changes in the volume and shape of the simulation cell based on isothermal–isobaric rigid molecule Monte Carlo (NPT–MC). The final configuration from the k th NPT–MC sequence and final velocities from the k th NVT–MD segment defined the initial point in phase space for $k + 1$ th NVT–MD/NPT–MC segment. Starting with $P = 0$ GPa, equilibration runs of length 0.2 ns (20 000 NPT–MC samples) were performed for each thermodynamic state considered. The initial phase space point for equilibration at successively higher pressures was taken from the equilibration run at the next lower pressure once it had reached steady-fluctuating values of the lattice parameters; the Monte Carlo step size was adjusted during the first 0.1 ns of equilibration to yield ~40% acceptance probability at a given thermodynamic state, after which it was held constant for the

duration of equilibration and production simulation for that state. Production runs comprised of 3.0 ns NVT–MD (300 000 NPT–MC observations) were performed for each thermodynamic state considered. A fixed time step of 1.0 fs was used.

Finally, gas-phase simulations were conducted using a Brownian dynamics integrator on an ensemble of molecules with intermolecular interactions turned off (i.e., an ideal molecular gas). Results of these simulations were used in calculating energies of sublimation and heat of vaporization.

V. MD Simulation Results Using the Many-Body Polarizable Force Field

A. Alkyl Nitrates and PETN Liquid. Densities, heats of vaporization, and self-diffusion coefficients for alkyl nitrates obtained from MD simulations using the many-body polarizable force field are shown in Table 5. Densities of ethyl nitrate and butyl nitrate are predicted to within 0.5% of experimental values, while for isopropyl nitrate, the density is in error by 2.5% compared with the experimental value. Interestingly, similar trends were observed for the COMPASS force field,⁶ where an error of 3.0% was obtained for the calculated density of isopropyl nitrate compared with experiment. The accuracy of the predicted heats of vaporization (errors of –1.5% to –6.9%) is typical of what is obtained from our quantum-chemistry-based transferable force fields¹⁵ and is similar to the description of heat of vaporization for alkyl nitrates reported for the COMPASS force field (errors of –2.0% to 5.8%).¹⁵ We note that the COMPASS repulsion/dispersion parameters were adjusted to reproduce thermodynamic data for alkyl nitrates, whereas our repulsion/dispersion parameters were taken without change from our previously developed quantum-chemistry-based force fields²⁴ for ethers, alkanes, and nitrogen-containing compounds. Predicted self-diffusion coefficients for alkyl nitrates are also reported in Table 5. We could find no experimental data for self-diffusion coefficients of alkyl nitrates for comparison. Finally, the density of PETN liquid at $T = 416$ K is reported in

TABLE 6: PETN Unit Cell Parameters and Phase Transition Energies

	unit cell properties				transition energies	
	<i>a</i> (Å)	<i>b</i> (Å)	<i>c</i> (Å)	<i>V</i> (Å ³)	sublimation at 298 K (kcal/mol)	melting at 416 K (cal/g)
PETN-I at 298 K						
MD (MB)	9.40	9.40	6.76	597.1	35.8	34
MD (TB)	9.32	9.32	6.86	596.0	36.7	33
MD (TB, flexible bonds)	9.34	9.34	6.86	598.1		
experiment	9.38 ^a	9.38 ^a	6.71 ^a	590.4 ^a	36 ^c , 37 ^d	38 ^e
PETN – II at 406 K						
MD (MB)	13.28	13.38	6.92	1231		
MD (TB)	13.18	13.30	7.00	1226		
experiment	13.29 ^b	13.49 ^b	6.83 ^b	1224 ^b		

^a Reference 37. ^b Reference 26. ^c Reference 10. ^d Reference 11. ^e Reference 26.

Table 5; it is about 1% higher than the calculated density of PETN-I crystal at the same temperature, indicative of a small volume change associated with melting.

B. PETN Crystal. Unit cell lattice parameters for PETN-I and PETN-II and the phase-transition energies for PETN-I obtained using the polarizable potential are given along with available experimental values for these quantities in Table 6. Excellent agreement (maximum |% error| ≤ 1.3%) was obtained for the unit cell parameters of both PETN crystal polymorphs. The energy of sublimation for PETN-I also matches the experimental value with high accuracy (−1.9% error); the heat of fusion is predicted to be 10.5% lower than the experimental value reported for single-crystal PETN.²⁶

The ability of MD simulations using the polarizable potential to predict the pressure dependence of unit cell parameters for the PETN-I polymorph was investigated and is presented in Figure 2. Good agreement with experiment is observed for cell parameters up to 7 GPa. The calculated *a* parameter exhibits a slightly weaker pressure dependence than experiment; this is compensated by a stronger pressure dependence of the *c* parameter such that the percent error in unit cell volume at 7 GPa is only 1%. The simulated results for PETN-I in this pressure interval indicate tetragonal symmetry on average. However, at pressures greater than 7 GPa, PETN transforms from tetragonal to orthorhombic symmetry, with a difference of less than 0.7% between time-averaged *a* and *b* parameters. As shown in Figure 2, imposition of tetragonal symmetry (*a* = *b*) during the simulation results in a small but reproducible discontinuity at *P* ~ 7 GPa in the values of the *c* parameter and unit cell volume. Above this transition pressure, the *c* parameter predicted using the polarizable force field deviates noticeably from experiment.

Both Raman²⁹ and X-ray²⁹ investigations of PETN under hydrostatic compression reveal that PETN deforms smoothly with no indication of a phase transformation. However, X-ray studies of PETN performed in a diamond-anvil cell in the absence of a hydrostatic medium, in which case complicated, uncontrolled shear stresses will exist within the sample volume, did reveal a phase change around 7 GPa.³⁰ Intriguingly, the pressure range of the structural transitions observed in our simulations, performed under hydrostatic compression without a compression medium, appear to be consistent with that observed in X-ray diffraction measurements performed under nonhydrostatic conditions. We defer a detailed investigation of the high-pressure phase transition observed in our simulations of PETN using the polarizable force field to future work.

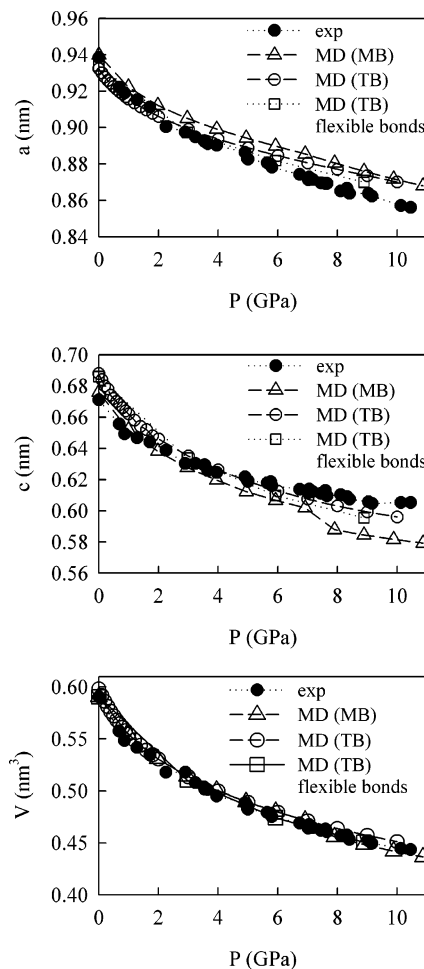


Figure 2. Pressure dependence of lattice lengths and unit cell volume for PETN-I at 298 K from MD simulations and X-ray scattering experiments.³⁷

VI. Development of a Two-Body Nonpolarizable PETN Force Field

Having validated the ability of the many-body polarizable force field to predict structural and thermodynamic properties of PETN and liquid alkane nitrates, we next developed a more computationally efficient two-body nonpolarizable force field. We assumed that repulsion/dispersion, bonding, bending, and torsional parameters are transferable directly from the polarizable version of the force field. Hence, the challenge in developing the two-body potential is to capture the influence of condensed-phase effects on electrostatic interactions without including explicitly the computationally expensive many-body atom-dipole polarizability. In order to meet this challenge, PETN partial charges in the nonpolarizable potential were fit to reproduce the electrostatic potential due to a polarized PETN molecule in the crystal environment of the polarizable force field. Specifically, an electrostatic grid was placed around 10 randomly chosen PETN molecules during an MD simulation of PETN-I crystal using the polarizable potential. Then, partial atomic charges for the nonpolarizable force field were fit by minimizing the functional χ^2 (eq 9) where in this case the objective potential is that due to the polarized PETN molecules obtained from simulations using the polarizable potential. The resulting partial atomic charges for the nonpolarizable force field are compared to those for the polarizable force field in Table 7.

An important advantage of the present approach for obtaining partial atomic charges for the nonpolarizable force field

TABLE 7: PETN Charges for Polarizable and Nonpolarizable Force Fields

element	type	charge (e)	
		polarizable	nonpolarizable
C	neopentyl	−0.2972	−0.3344
C	nitrate	0.1308	0.3034
H		0.1063	0.0687
O	nitro	−0.3856	−0.4020
O	nitrate	−0.2879	−0.4171
N		0.7900	0.8642

compared to fitting charges to the electrostatic potential obtained from gas-phase calculations is that the charges obtained this way capture directly, in a mean-field sense, the influence of condensed-phase polarization on electrostatic interactions. When charges for nonpolarizable potentials are determined from the electrostatic potential surrounding gas-phase molecules, particularly for highly polar molecules, it is often necessary to scale (typically increase) the gas-phase partial charges to account for condensed phase polarization effects present in liquid and solid phases. The extent of charge scaling is usually arbitrary and empirical, for example, adjusting the scaling to reproduce a particular property such as liquid-phase density or crystal unit cell parameters.

VII. Simulation Results for the Nonpolarizable Force Field

A. Unit Cell Parameters and Phase Transitions. Predicted unit cell parameters, heat of fusion, and energy of sublimation for PETN crystal using the nonpolarizable potential are compared to experiment and values obtained using the many-body polarizable potential in Table 6. MD simulations using the nonpolarizable force field predict slightly smaller *a* and *b* parameters than simulations using the polarizable force field while the *c* parameter with the nonpolarizable force field is slightly larger than the prediction of the polarizable force field. The largest discrepancy is 1.5%, for *c* in PETN-I. The pressure dependence of the cell parameters and unit cell volume are in good agreement with experiments as shown in Figure 2. Interestingly, the simulations using the nonpolarizable potential do not indicate a phase transition anywhere in the pressure interval studied (0–10 GPa), in contrast to what was found for the polarizable potential. The energy of sublimation and heat of fusion obtained from simulations using the nonpolarizable force field differ by 2.5% and 3.0%, respectively, from those observed for the polarizable force field but are still in acceptable agreement with experimental data (errors of 0.9% and −1.3%, respectively).

The sensitivity of the predicted PETN hydrostatic compression with and without constrained bonds was investigated by calculating unit cell parameters in the pressure interval 0–10 GPa. Results for PETN-I with flexible bonds are shown in Table 6 for 1 atm and as a function of pressure in Figure 2. From the results in Table 6, it is seen that the unit cell parameters *a*, *b*, and *c* of PETN at 1 atm differ by less than 0.16% for flexible versus constrained bonds. Figure 2 indicates that the flexible model is detectably more compressible, but unit cell parameters from simulations at 9 GPa using constrained and flexible bonds differ by less than 0.5%. Thus, we conclude that constraining the bond lengths in PETN does not introduce significant effects in the interval of pressures studied. This result is consistent with the results of quantum chemistry predictions for the hydrostatic compression of PETN crystal.³¹

B. Elastic Coefficients. The full set of isothermal elastic constants (C_{ij}) and isotropic bulk (*K*) and shear (*G*) moduli for

TABLE 8: Elastic Coefficients for PETN-I

elastic coefficient ^a (GPa)	MD–MC (nonpolarizable)	experiment ^b (ref 13)
C_{11}	17.5 ± 0.2	
C_{22}	17.7 ± 0.1	
$\langle C_{11} + C_{22} \rangle$	17.6 ± 0.2	17.22
C_{33}	10.5 ± 0.1	12.17
C_{44}	4.60 ± 0.04	
C_{55}	4.72 ± 0.02	
$\langle C_{44} + C_{55} \rangle$	4.66 ± 0.03	5.04
C_{66}	4.92 ± 0.03	3.95
C_{12}	4.7 ± 0.1	5.44
C_{13}	6.5 ± 0.1	
C_{23}	6.8 ± 0.1	
$\langle C_{13} + C_{23} \rangle$	6.65 ± 0.1	7.99
K_{Reuss}	8.7 ^c	9.1 ^{d,e}
G_{Reuss}	4.3 ^c	3.8 ^{d,e}
K_{Voigt}	9.1 ^e	9.1
G_{Voigt}	4.7 ^e	3.8
K_{isotherm}	8.4 ^f	
$K'_{\text{isotherm}} = dK_{\text{isotherm}}/dP$	13.0 ^f	

^a Isothermal elastic tensor was computed within a triclinic simulation protocol; thus, all nine nonzero values are reported; averaged values for symmetry-equivalent pairs (i.e., C_{11} and C_{22} , C_{44} and C_{55} , C_{13} and C_{23}) are reported in brackets [...] for comparison to experimental values.

^b Isotropic values. ^c Obtained from the compliance tensor, $\mathbf{S} = \mathbf{C}^{-1}$, see ref 2. ^d Isotropic values derived from C_{ij} in ref 13 were adjusted here to obtain approximate isothermal values using $K_T = K_s(C_v/C_p) \sim 0.926K_s$, where subscripts *T* and *s* denote isothermal and isentropic values, respectively, and C_v/C_p is the ratio of constant volume and constant pressure specific heats. ^e Obtained from the stiffness tensor, see ref 2. ^f From a fit of the calculated isotherm to the third-order Birch–Murnaghan equation of state in the (*P*,*V*) plane, with all 24 points weighted equally; dimensionless.

PETN-I calculated at 298 K and 1 atm using the nonpolarizable potential in conjunction with the Parrinello–Rahman strain–strain fluctuation formula² are reported in Table 8. The calculated isothermal elastic tensor conforms closely to the expected form for a tetragonal system for which, in the present case, we expect $C_{11} = C_{22}$, $C_{44} = C_{55}$, and $C_{13} = C_{23}$; these are satisfied within 4.5%. Winey and Gupta¹³ have performed a re-analysis of earlier sound speed measurements due to Morris³² and reported what is thought to be an accurate, precise, and internally consistent isentropic elastic tensor. A recent determination based on Brillouin scattering from acoustic phonons is in essential agreement with a systematic difference of ~4%.³³ The Winey–Gupta results are included in the right-hand column of Table 8, with no attempt to transform them from isentropic to isothermal values (the isentropic values should be larger than the isothermal ones by a few percent). The comparison is quite good: the average unsigned and signed percent errors between the calculated and the measured 6 independent values are only −4.1% and 13.1%, respectively. This level of agreement between predicted and measured elastic coefficients is rare for such complicated organic materials⁵ and constitutes a particularly strong validation metric for the nonpolarizable PETN force field.

Isotropic bulk and shear moduli were calculated for the predicted and measured elastic coefficients using expressions for the Reuss (uniform stress) and Voigt (uniform strain) bounds.² These values are included in Table 8. In this case, we performed an approximate transformation of the isentropic values derived from the experimental elastic tensor and its matrix inverse, the compliance tensor; namely, $x_T = x_S(C_v/C_p)$, where *T* and *s* denote isothermal and isentropic conditions, respectively, and C_v/C_p is the ratio of specific heats under conditions of constant volume and constant pressure (0.926 from ref 34). The Reuss bound should always be less than or equal to the Voigt

bound and is the one that should be compared to isotropic bulk modulus values obtained from equation of state fits to hydrostatic compression data.

VIII. Conclusions

A transferable flexible molecule quantum-chemistry-based many-body polarizable force field has been developed for alkyl nitrates and PETN. No experimental information on those compounds was used in the parametrization of the force field. MD simulations using this force field predicted accurate lattice parameters for two PETN crystal polymorphs, pressure dependencies of PETN-I lattice parameters up to 7 GPa, and heats of sublimation and melting. The force field also yielded accurate predictions compared to experiment for the available thermodynamic properties of alkyl nitrates.

We also presented a nonpolarizable two-body force field for PETN based on results obtained from simulations of the crystal using the many-body polarizable force field. Specifically, we determined a set of partial charges for the nonpolarizable force field by fitting simultaneously the electrostatic potential, dipole moments, and quadrupole moments of PETN molecules located in a PETN crystal described by the polarizable version. This approach to obtaining partial charges for nonpolarizable force fields is more rigorous than the usual approach of fitting charges based on gas-phase results and then uniformly scaling them to account empirically for condensed-phase effects.

Simulations using the nonpolarizable force field provided accurate predictions of thermophysical/mechanical properties of PETN crystal on the room-temperature isotherm. The nonpolarizable version of the force field for PETN is preferable to the polarizable one for prediction of bulk properties since it provides results of comparable quality at significantly reduced computational expense. By contrast, the polarizable version of the force field is expected to be useful for prediction of accurate interfacial properties. Finally, it was shown explicitly that the choice between constrained versus flexible bonds in the simulations has a negligible influence on the PETN structural properties calculated at 298 K for pressures less than 9 GPa.

Acknowledgment. Wasatch Molecular Incorporated acknowledges financial support from Sandia National Laboratories (SNL). SNL is a multiprogram laboratory operated by Sandia Corporation, a Lockheed Martin company, for the United States Department of Energy under Contract No. DE-AC04-94AL85000. T.D.S. is supported by the High Explosives Project of the Advanced Strategic Computing Program at Los Alamos National Laboratory, operated by Los Alamos National Security L.L.C. under the auspices of the National Nuclear Security Administration of the United States Department of Energy under Contract No. DE-AC52-06NA25396. G.D.S. is partially supported by the University of Utah Center for the Simulation of Accidental Fires and Explosions (C-SAFE), funded by the Department of Energy, Lawrence Livermore National Laboratory, under subcontract B341493.

Appendix

Property Calculations from MD Simulations. *Energy of Sublimation and Heat of Vaporization.* The energy of sublimation and heat of vaporization were calculated using eqs a1 and a2, respectively.

$$\Delta U^{\text{sub}} = U^{\text{crystal}} - U^{\text{vap}} \quad (\text{a1})$$

$$\Delta H = U^{\text{liq}} - U^{\text{vap}} + RT \quad (\text{a2})$$

where U^{crystal} is the potential energy of a crystal; U^{liq} and U^{vap} are the energies of liquid and gas phases, respectively; R is the gas constant, and T is temperature. The gas-phase energy was calculated in MD simulations using a Brownian dynamics algorithm with no intermolecular interactions (ideal gas assumption).

Self-Diffusion Coefficient. The self-diffusion coefficient (D) was calculated using the Einstein relation,

$$D = \lim_{t \rightarrow \infty} \frac{\langle \text{MSD}_i(t) \rangle}{6t} \quad (\text{a3})$$

where $\text{MSD}(t)$ is the mean-square displacement of the center of mass of a molecule during time t ; $\langle \rangle$ denotes an ensemble average.

Elastic Coefficients. Elastic coefficients were obtained using the strain-strain fluctuation formula due to Rahman and Parrinello for the elastic compliance tensor as described in our previous works.² The full set of 300 000 NPT-MC observations was considered to compute the elastic tensor, using a bootstrap algorithm to yield uncertainty estimates for the individual C_{ij} .² Specifically, the elastic tensor was computed by randomly sampling (with replacement) 30 000 of the 300 000 NPT-MC observations to yield one value for the microscopic strain. This was repeated 10 times so that, on average, each NPT-MC observation was used only once in the analysis. The elastic coefficients reported in Table 8 are the element-by-element mean values from the 10 independent bootstrapped realizations, while the uncertainties are the simple standard deviations of those element-by-element mean values.

Supporting Information Available: Energies and geometries for investigated conformers and the distortion of the nitrate group in ethyl nitrate. This material is available free of charge via the Internet at <http://pubs.acs.org>.

References and Notes

- (1) Rice, B. M.; Byrd, E. F. C. *J. Mater. Res.* **2006**, *21*, 2444.
- (2) Sewell, T. D.; Menikoff, R.; Bedrov, D.; Smith, G. D. *J. Chem. Phys.* **2003**, *119*, 7417.
- (3) Bedrov, D.; Borodin, O.; Hanson, B.; Smith, G. D. *J. Phys. Chem. B* **2007**, *111*, 1900.
- (4) Jaramillo, E.; Sewell, T. D.; Strachan, A. *Phys. Rev. B* **2007**, *76*.
- (5) Day, G. M.; Price, S. L.; Leslie, M. *Cryst. Growth Des.* **2001**, *1*, 13.
- (6) Bunte, S. W.; Sun, H. *J. Phys. Chem. B* **2000**, *104*, 2477.
- (7) Ye, S.; Tonokura, K.; Koshi, M. *Sci. Tech. Energ. Mater.* **2003**, *64*, 201.
- (8) Zaoui, A.; Sekkal, W. *Solid State Commun.* **2001**, *118*, 345.
- (9) Sorescu, D. C.; Rice, B. M.; Thompson, D. L. *J. Phys. Chem. B* **1999**, *103*, 6783.
- (10) Cundall, R. B.; Palmer, T. F.; Wood, C. E. C. *J. Chem. Soc., Faraday Trans.* **1978**, *74*, 1339.
- (11) Lau, K. H.; Hildenbrand, D. L.; Crouch-Baker, S.; Sanjurjo, A. *J. Chem. Eng. Data* **2004**, *49*, 544.
- (12) Gee, R. H.; Wu, C.; Maiti, A. *Appl. Phys. Lett.* **2006**, *89*, 021919.
- (13) Winey, J. M.; Gupta, Y. M. *J. Appl. Phys.* **2001**, *90*, 1669.
- (14) Halgren, T. A. *J. Am. Chem. Soc.* **1992**, *114*, 7827.
- (15) Borodin, O.; Smith, G. D. *J. Phys. Chem. B* **2006**, *110*, 6279.
- (16) Geerke, D. P.; van Gunsteren, W. F. *J. Phys. Chem. B* **2007**, *111*, 6425.
- (17) Frisch, M. J.; Trucks, G. W.; Schlegel, H. B.; Scuseria, G. E.; Robb, M. A.; Cheeseman, J. R.; Zakrzewski, V. G.; Montgomery, J. A., Jr.; Stratmann, R. E.; Burant, J. C.; Dapprich, S.; Millam, J. M.; Daniels, A. D.; Kudin, K. N.; Strain, M. C.; Farkas, O.; Tomasi, J.; Barone, V.; Cossi, M.; Cammi, R.; Mennucci, B.; Pomelli, C.; Adamo, C.; Clifford, S.; Ochterski, J.; Petersson, G. A.; Ayala, P. Y.; Cui, Q.; Morokuma, K.; Malick, D. K.; Rabuck, A. D.; Raghavachari, K.; Foresman, J. B.; Cioslowski, J.; Ortiz, J. V.; Stefanov, B. B.; Liu, G.; Liashenko, A.; Piskorz, P.; Komaromi, I.; Gomperts, R.; Martin, R. L.; Fox, D. J.; Keith, T.; Al-Laham, M. A.; Peng, C. Y.; Nanayakkara, A.; Gonzalez, C.; Challacombe, M.; Gill, P. M. W.; Johnson, B. G.; Chen, W.; Wong, M. W.; Andres, J. L.; Head-Gordon,

M.; Replogle, E. S.; Pople, J. A. *Gaussian 98*, revision A.7; Gaussian, Inc.: Pittsburgh, PA, 1998.

(18) Zhao, Y.; Truhlar, D. G. *J. Chem. Theory Comput.* **2005**, *1*, 415.

(19) Gruzdkov, Y. A.; Dreger, Z. A.; Gupta, Y. M. *J. Phys. Chem. A* **2004**, *108*, 6216.

(20) Borodin, O.; Smith, G. D. *J. Phys. Chem. B* **2003**, *107*, 6801.

(21) Borodin, O.; Smith, G. D. *J. Phys. Chem. B* **2006**, *110*, 6293.

(22) Smith, G. D.; Borodin, O. Quantum Chemistry-Based Force Fields for Polymers. In *Molecular Simulation Methods for Predicting Polymer Properties*; Galiatsatos, V., Ed.; Wiley: New York, 2005; p 1–45.

(23) Borodin, O.; Smith, G. D. *J. Phys. Chem. B* **2006**, *110*, 11481.

(24) Borodin, O., 2007, unpublished results.

(25) Ayyagari, C.; Smith, G. D.; Bedrov, D.; Borodin, O. *Lucretius*; <http://www.eng.utah.edu/~gdsmith/>.

(26) Cady, H. H.; Larson, A. L. *Acta Cryst.* **1975**, *B31*, 1864.

(27) Frenkel, D.; Smit, B. *Understanding Molecular Simulation: From Algorithms to Applications*, 2nd ed.; Academic Press: New York, 2002.

(28) Martyna, G. J.; Tuckerman, M.; Tobias, D. J.; Klein, M. L. *Mol. Phys.* **1996**, *87*, 1117.

(29) Lipinska-Kalita, K. E.; Pravica, M. G.; Nicol, M. *J. Phys. Chem. B* **2005**, *109*, 19223.

(30) Pravica, M.; Lipinska-Kalita, K.; Quine, Z.; Romano, E.; Shen, Y.; Nicol, M. F.; Pravica, W. J. *J. Phys. Chem. Solids* **2006**, *67*, 2159.

(31) Gan, C. K.; Sewell, T. D.; Challacombe, M. *Phys. Rev. B* **2004**, *69*, 7.

(32) Morris, C. E. In *Sixth Symposium (International) on Detonation*; Edwards, D. J., Ed.; Washington, DC, 1976; p 396.

(33) Stevens, L. L.; Dattelbaum, D. M., 2007, private communication to Sewell, T. D.

(34) Olinger, B.; Cady, H. *Proc. 6th Symp. (Int.) on Detonation*; Office of Naval Research: Arlington, VA, 1976; 700.

(35) *The CRC Handbook of Chemistry and Physics*; 2006; <http://www.hbcpnetbase.com/>.

(36) Gray, P.; T., P. M. W. *J. Chem. Soc.* **1957**, 2163.

(37) Olinger, B.; Halleck, P. M.; Cady, H. H. *J. Chem. Phys.* **1975**, *62*, 4480.